International Journal of Heat and Mass Transfer 131 (2019) 463–471

Contents lists available at ScienceDirect

International Journal of Heat and Mass Transfer

journal homepage: www.elsevier.com/locate/ijhmt

Large eddy simulation analysis of the heat transfer enhancement using self-oscillating fluidic oscillators

Yongjia Wu, Shifeng Yu, Lei Zuo *

Department of Mechanical Engineering, Virginia Tech, Blacksburg, VA 24061, USA

ARTICLE INFO

Article history:
Received 17 August 2018
Received in revised form 14 November 2018
Accepted 14 November 2018
Available online 22 November 2018

Keywords:
Fluidic oscillator
Fluid dynamics
Heat transfer
Large eddy simulation

ABSTRACT

Using an unsteady jet created by the fluidic oscillator represents many opportunities to enhance the heat removal performance of impinging jet. Numerical simulations were conducted to compare the heat transfer performance of two fluid oscillators and a direct jet with unsteady Reynolds-averaged Navier-Stokes (RANS) and large eddy simulation (LES) turbulence models implemented. Time-resolved and time-averaged flow fields and heat transfer results were presented. Simulation results showed that the fluid dynamic and heat transfer performance predicted by the RANS and LES models matched well for different Reynolds numbers.The self-oscillating impinging jets were beneficial in enhancing the heat removal performance by increasing the average Nusselt numbers and covering a larger impinging cooling surface. The wide impinging zone and significant heat transfer enhancement suggested it was promising to implement self-oscillating impinging jet concept into existing cooling technologies, such as multi-phase cooling and thin film cooling, for the next-generation high-performance heat exchangers.

1. Introduction

The fluidic oscillator is a unique device that can convert a steady state jet into an oscillatory one based on the intrinsic flow instability mechanisms. The attractive feature of a fluidic oscillator for flow control is its characteristics of unsteady blowing, which can be used to actively manipulate the flow field without any moving parts. The fluidic oscillator was widely used in flow separation control [1,2], jet thrust vectoring [3], cavity tone suppression [4], drag reduction [5], combustion control [6] and heat transfer enhancement [7–10]. Numerous designs have been proposed since it originated from the 1960s [11]. Generally, the fluidic oscillators can be categorized into two types [12]: wall-attachment and jet-interaction oscillators [13] regarding the driven mechanisms of the oscillations. The wall-attachment type with two feedback channels, as shown in Fig. 1, is the most often studied one and will be adopted for the analysis in this paper.

A typical wall-attachment fluidic oscillator includes a power nozzle, a main mixing chamber, two feedback channels, and an exit throat. Though the general working principles of the fluidic oscillators were well documented in various literature [9,12], the detailed flow physics of these devices were not. The power jet coming out from the power nozzle will attach to one of the two side walls of the mixing chamber due to the Coanda effect [12,14]. As the flow field is not symmetric, the fluid mass rates entering into the two feedback loops are different. This transverse disturbance leads to a change in the pressure through the control nozzles, which drives the power jet to detach from the original sidewall and attach to the opposite sidewall. Due to the symmetry of the device, the same process repeats resulting in an oscillatory fluid motion at the exit throat. Previous research [15] found that fluidic oscillators were robust in a wide range of operating conditions.

The fluid dynamic characteristics of the fluidic oscillators, such as the oscillation frequency, pressure variation, and oscillating amplitude, were intensively studied in many open literature [16–23]. Seo et al. [17] used a 2-D dimensional model to investigate the internal fluid dynamics of a fluidic oscillator by solving the incompressible Navier–Stokes equations. They analyzed the influence of geometric variations including changes in the feedback channel length and the mixing chamber length on the oscillation frequency and amplitude. Woszidlo and Wygnanski [1] experimentally and numerically investigated the parameters governing separation control using an array of sweeping jet actuators distributed evenly along the span of a generic airfoil. They found that by controlling separation, actuation still yielded almost twice the range of lift coefficients accompanied by almost twice the maximum lift-to-drag ratio. Metka and Gregory [5] experimentally studied drag reduction on the 25-deg Ahmed generic vehicle model with quasi-steady blowing at the roof–slant interface using

* Corresponding author.
E-mail address: leizuo@vt.edu (L. Zuo).

https://doi.org/10.1016/j.ijheatmasstransfer.2018.11.070
0017-9310/

Nomenclature

Symbols

D, D_f	characteristic length (m)
Nu	Nusselt number
q'	heat flux ($W \cdot m^{-2}$)
h	convective heat transfer coefficient ($W \cdot m^{-2} \cdot K^{-1}$)
ρ	density ($kg \cdot m^{-3}$)
U_0	inlet velocity ($m \cdot s^{-1}$)
u_i	velocity ($m \cdot s^{-1}$)
t	time (s)
τ_{ij}, T_{ij}	Reynolds stresses ($kg \cdot m^{-1} \cdot s^{-2}$)
μ	dynamic viscosity ($kg \cdot m^{-1} \cdot s^{-1}$)
c_p	thermal capacity ($J \cdot kg^{-1} \cdot K^{-1}$)
T	temperature (K)
T_f	oscillating period (s)
λ	thermal conductivity ($W \cdot K^{-1} \cdot m^{-2}$)
S_i	energy source terms ($W \cdot s^{-1}$)
k	turbulence kinetic energy (J/kg)
μ_t	Eddy viscosity ($kg \cdot m^{-1} \cdot s^{-1}$)
ω	turbulence frequency (s^{-1})
S_{ij}	mean rate of deformation (s^{-1})
δ_{ij}	Kronecker delta
σ_k, β^*, $\sigma_{\omega,2}$, γ_2, β_2	factors in the k-ω SST turbulence model
$\sigma_{\omega,1}$	turbulence frequency Prandtl number
Δ_1, Δ_2	filtering length (m)
C_{SGS}	factors in the LES model
L_{ij}	Germano identity
M_{ij}	intermediate parameter

Abbreviations

RANS	Reynolds-averaged Navier-Stokes
LES	large eddy simulation
ELES	embedded large eddy simulation
SST	shear stress transport
CFD	computational fluid dynamic
SGS	sub-grid-scale stresses
SIMPLE	semi-implicit method for pressure linked equations
CFL	Courant–Friedrichs–Lewy condition

a span-wise array of fluidic oscillators. A drag reduction up to 7.5% was observed on the model with the actuation. The reduction was due to separation control on the slant surface. Jeong and Kim [24] optimized the 3-D geometry shape of a fluidic oscillator by solving the transient Reynolds-averaged Navier-Stokes (RANS) equations to enhance peak jet velocity at the exit throat and simultaneously reduce pressure drop. Bobusch et al. [19] did experiments to investigate the internal flow characteristics of a fluidic oscillator. Geometrical features, in particular at the inlet and outlet of the mixing chamber, were found to have crucial impacts on oscillation frequency and jet deflection. Choephel et al. [25] conducted experiments to explore the use of fluidic oscillators for improving the aerodynamic performance of the S903 airfoil. The increase in lift coefficient ranged from 10% to 20% depending on the Reynolds number. The actuation level was studied in the experiments. The same phenomenon was observed in the work by DeSalvo et al. [26]. Guyot et al. [6] used a fluidic oscillator as an actuator to do fuel modulation. The oscillator was incorporated into a bluff body burner to examine the influence on the combustion stability. Cattafesta and Sheplak [15] gave a detailed review on using fluidic oscillators for active flow control.

Most of the research on fluidic oscillators focused on their fluid dynamic performance. Using sweeping jet impingement caused by the fluidic oscillator for heat transfer enhancement application is still relatively new. Jet impingement is an effective way to cool device working in high-temperature environment, such as vane leading edge cooling in gas turbine [10]. However, steady jet impingent can only effectively cool a hot spot, as the Nusselt number decreases drastically from the stagnation point to the sides. The sweeping jet has great potential enhancing impingement heat transfer through its larger spreading angle and regions of high turbulent mixing due to the sweeping nature of the flow at the exit throat. There is a great potential to implement the present self-oscillating-impinging-jet concept in future gas turbine cooling systems, electronics cooling, multi-phase cooling, micro-fluid cooling, and thin film cooling. Camci and Herr [8] first used a self-oscillating-impinging-jet configuration to enhance the heat removal performance of the impinging jets. The new design significantly enhanced the heat transfer coefficient ranging from 20% to 70% over the stationary jet values because of the oscillation motion of the impinging jet together with the larger impingement zone. Hossain et al. [10] developed a sweeping jet film cooling technology based on conventional curved fluidic oscillators to improve the cooling effect of gas turbine engines. Both experimental and numerical studies were conducted to test the performance of a row of five sweeping jet film cooling holes. They found that the unsteady sweeping action of the jet augmented the heat transfer near the hole exit. In another paper [9], they used unsteady RANS simulations to analyze the effects of surface curvature on the performance of sweeping jet impingement heat transfer. Agricola et al. [7] compared the heat transfer coefficient of a sweeping impinging jet to a steady circular orifice jet. They found that impingement

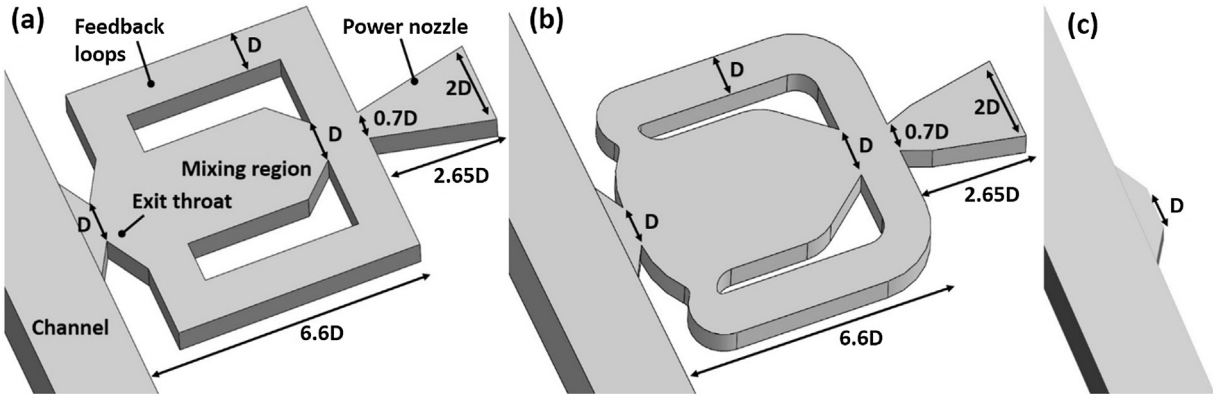

Fig. 1. (a) The angled fluidic oscillator, (b) The curved fluidic oscillator, (c) The direct jet.

heat transfer using a sweeping jet was better at high Reynolds numbers. Park et al. [27] experimentally examined the heat transfer of a sweeping jet impinging on a flat wall for several Reynolds number and nozzle-to-plate spacings. Compared to a steady round jet, the sweeping jet showed the superior capability of heat transfer.

The self-oscillating impinging jet has great potential to be implemented in future high-performance multi-phase cooling, modern electronic cooling, and compact heat exchangers. Though much progress was made in recent years, using fluidic oscillators for heat removal was still not fully explored. For example, in Refs. [27,7], the conclusions on the heat transfer enhanced using self-oscillating impinging jet for low *Re* numbers ($Re < 10{,}000$) were not consistent. These can be reasoned as follows. On one hand, to accurately measure the convective heat coefficients was by no means an easy task. On the other hand, the two-equations RANS turbulence model, for example the commonly used $k-\omega$ SST model, might overestimate the heat convective coefficients for direct jets [28]. In this paper, the heat removal performance of two commonly used 3D fluidic oscillators [23], a curved one and an angled one, were compared using two turbulence models, including the transient RANS $k-\omega$ SST turbulence model and the embedded large eddy simulation (ELES) turbulence model [29]. The curved oscillator design was used in many Refs. [3,4,7,19,23,30] and the angled oscillator design was used in some others [2,16,21,23]. The ELES model uses the RANS model to simulate the regions that are less important and large eddy simulation (LES) model for the regions of interest. In this way, the ELES model preserves the turbulence resolution of LES model without introducing much additional computation cost. The water rather than air was selected as the working fluid here since water has higher heat removal performance though it was harder to manipulate the range of its *Re* numbers in real experiments.

2. Computational method

2.1. Fluidic oscillators

In this study, the geometry of the angled fluidic oscillator was scaled from the computational model used in Ref. [16] and the geometry of the curved one was adjusted from Ref. [23]. The 3-D geometry information of the fluidic oscillators was shown in Fig. 1. The overall size (25 mm × 11.25 mm × 1.5 mm) of the two devices were the same. The width of the inlets was 2D (where D = 1.0 mm in both designs). The thickness of the fluidic oscillator was 0.5D and the thickness of the fluid channel was 1.5D. The outlet of the channel was 12.5D away from the center of the throat to make sure the outlet boundary condition would not significantly affect the fluid dynamics of the sweeping jet. The angle and width of the outlet throat were the same for the two models. Besides, a direct jet model was also established (by removing the feedback loops of the fluidic oscillator) to act as a reference. The simulation was performed using water with $Re = 3000$, 4000, and 5000, respectively.

2.2. Numerical model

2.2.1. The $k-\omega$ SST model

The flows through the fluidic oscillators were simulated by solving the incompressible Navier–Stokes equations. The $k-\omega$ SST model and the ELES model were used to simulate the turbulence separately. The $k-\omega$ SST model developed by Menter et al. [31,32] is thought to be robust to fit turbulence for a wide *Re* number range. By introducing the blending functions, this model combines the good near-wall behavior of the $k-\omega$ model with the robustness of the $k-\varepsilon$ model in the far field in a numerically stable way. However, previous studies showed that the $k-\omega$ SST model tended to overpredict the *Nu* number near the impingement zone [28]. The governing equations of the transitional $k-\omega$ SST model are prescribed by:*Continuity equation*

$$\frac{\partial(\rho)}{\partial t}+\frac{\partial(\rho u_j)}{\partial x_j}=0 \tag{1}$$

Momentum equations

$$\frac{\partial(\rho u_i)}{\partial t}+\frac{\partial(\rho u_i u_j)}{\partial x_j}=-\frac{\partial p}{\partial x_i}+\frac{\partial \tau_{ij}}{\partial x_j}+\frac{\partial}{\partial x_j}\left(\mu\frac{\partial u_i}{\partial x_j}\right) \tag{2}$$

where $\tau_{ij}=-\rho\overline{u_i'u_j'}=2\mu_t S_{ij}$, S_{ij} is the mean rate of strain tensor.

Energy equation

$$\frac{\partial(\rho c_p T)}{\partial t}+\frac{\partial(\rho c_p u_j T)}{\partial x_j}=\frac{\partial}{\partial x_j}\left(\lambda\frac{\partial T}{\partial x_j}\right)-\tau_{ij}\frac{\partial u_i}{\partial x_j}+S_i \tag{3}$$

The k equation

$$\frac{\partial(\rho k)}{\partial t}+\frac{\partial(\rho k u_j)}{\partial x_j}=\frac{\partial\left(\left(\mu+\frac{\mu_t}{\sigma_k}\right)\frac{\partial k}{\partial x_i}\right)}{\partial x_j}+\left(\tau_{ij}\cdot S_{ij}-\frac{2}{3}\rho k\frac{\partial u_i}{\partial x_j}\delta_{ij}\right)-\beta^*\rho k\omega \tag{4}$$

The ω equation

$$\begin{aligned}\frac{\partial(\rho\omega)}{\partial t}+\frac{\partial(\rho\omega u_j)}{\partial x_j}=&\frac{\partial\left(\left(\mu+\frac{\mu_t}{\sigma_{\omega,1}}\right)\frac{\partial\omega}{\partial x_i}\right)}{\partial x_j}\\&+\gamma_2\left(2\rho S_{ij}\cdot S_{ij}-\frac{2}{3}\rho\omega\frac{\partial u_i}{\partial x_j}\delta_{ij}\right)-\beta_2\rho\omega^2\\&+2\frac{\rho}{\sigma_{\omega,2}\omega}\frac{\partial k}{\partial x_k}\frac{\partial\omega}{\partial x_k}\end{aligned} \tag{5}$$

where the σ_k, β^*, $\sigma_{\omega,2}$, γ_2 and β_2 are revised constants, with the corresponding values 2.0, 0.009, 1.17, 0.44, and 0.083, respectively. μ_t and $\sigma_{\omega,1}$ are related to the blending functions [29] to make the equations suitable for both the near wall and far field region.

2.2.2. The ELES model

Large eddy simulation is thought to be more accurate than transient RANS models, as it only models the sub-grid-scale turbulence. However, LES had the very limited impact on industrial CFD simulations, mainly due to its high computational cost. In order to preserve the resolution of large turbulent structures in industrial flow simulations, zonal models are desirable in many cases, where LES model is applied in the regions with high turbulence intensity and RANS model is used for regions of less interest. The information in the RANS and LES regions is exchanged at the interfaces using suitable methods. In this way, the combination of RANS and LES obviates the need to specify the inlet boundary condition for the LES simulation. ELES model was adopted to simulate the fluid dynamics of the sweeping jet in this study. In the power nozzle, two feedback loops, and channel far away from the sweeping jet, the $k-\omega$ SST model was used to save the computational cost. In the exit throat and the regions of the sweeping jet, the dynamic Smagorinsky model was used to obtain more accurate fluid dynamics and heat transfer results. At the LES-RANS interfaces, vortex method was used to generate a time-dependent inlet condition for the LES region. The combination of these two models was illustrated in Fig. 2.

The dynamic Smagorinsky model was developed based on the standard Smagorinsky model by Germano et al. [28] and Lilly et al. [33]. The local values of C_{SGS}, a coefficient in the eddy-viscosity model equation, is dynamically computed based on the information provided by the resolved scales of fluid motion. Taking

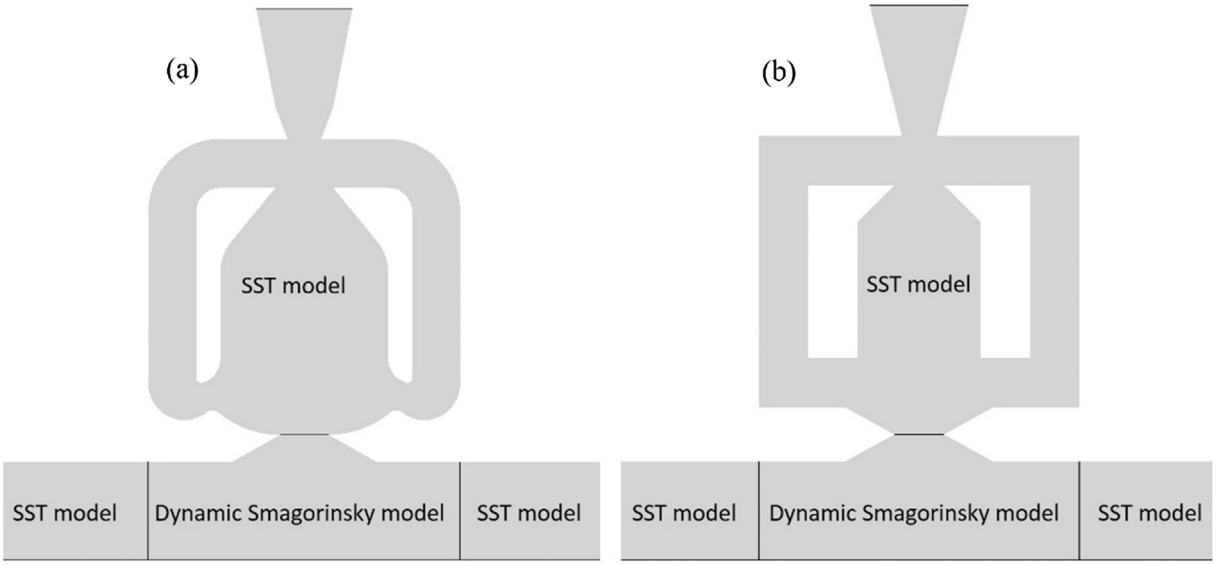

Fig. 2. Different turbulence models used in different regions in the fluidic oscillators.

the SGS stresses to be proportional to the stresses due to eddies at the smallest resolved scale, the SGS stress tensors using two different filtering length, Δ_1 and Δ_2 ($\Delta_2 > \Delta_1$), are modeled in the same way with the Smagorinsky-Lilly model.

$$\tau_{ij} = -2C_{SGS}^2\rho\Delta_1^2|\bar{S}|\left(\overline{S_{ij}} - \frac{1}{3}\overline{S_{kk}}\delta_{ij}\right) \tag{6}$$

$$T_{ij} = -2C_{SGS}^2\rho\Delta_2^2|\tilde{\bar{S}}|\left(\widetilde{\overline{S_{ij}}} - \frac{1}{3}\widetilde{\overline{S_{kk}}}\delta_{ij}\right) \tag{7}$$

where $\bar{S} = \sqrt{2\overline{S_{ij}}\overline{S_{ij}}}$. In Eqs. (6) and (7), the bar overhead represents for the first filtering operation with Δ_1 (the grid filter). The tilde overhead represents for the filtering operation with Δ_2 (the test filter).

The grid filtered SGS and the test-filtered SGS are related by the Germano identity [28],

$$L_{ij} = T_{ij} - \tilde{\tau}_{ij} \tag{8}$$

L_{ij} in Eq. (8) can be computed from the resolved large eddy field using

$$L_{ij} = \widetilde{\overline{u_i}}\widetilde{\overline{u_j}} - \widetilde{\overline{u_i}\overline{u_j}} \tag{9}$$

Substituting Eq. (7) and grid-filter Eq. (6) into Eq. (8), the constant C_{SGS}^2 can be calculated by

$$C_{SGS}^2 = \frac{\langle L_{ij} - L_{kk}\delta_{ij}/3\rangle}{\langle M_{ij}M_{ij}\rangle} \tag{10}$$

where $M_{ij} = -2\left(\Delta_2^2|\tilde{\bar{S}}|\widetilde{\overline{S_{ij}}} - \Delta_1^2|\bar{S}|\widetilde{\overline{S_{ij}}}\right)$. During the simulation, C_{SGS}^2 might become negative. To avoid numerical instability, both the numerator and the denominator in Eq. (10) are locally averaged using the test-filter. The dynamic Smagorinsky model was proved to be a robust eddy-viscosity model which was able to predict the turbulence near the wall and far field with good accuracy [31].

2.2.3. Numerical methodology

The fluid dynamic analysis of the fluidic oscillator was carried out using the ANSYS/FLUENT 14.0 package. The grid numbers for the curved fluidic oscillator, the angled fluidic oscillator, and direct fluidic oscillators were 8.80, 8.18, and 5.5 million, respectively. The grids at the boundary were adjusted to ensure that the dimensionless distance (y+) between the wall and the cell center of the first-layer grids near the walls were around 1.0. The grid quality was well checked to ensure better convergence (Fig. 3). The SIMPLE algorithm was used to solve the unsteady Navier-Stokes equations in a segregated manner. The Gauss-Green method was used for the pressure discretization. The discretization method used for all the other parameters was the second-order upwind method to ensure numerical stability. A second order implicit method was used in the time domain with a time step of 10^{-6} s to obtain time-resolved flow fields and heat transfer results. The time step was estimated by the averaged velocity at the throat of the nozzle, where the flow mean velocity was high, to ensure the CFL number less than 1.0 in the computational domain. In each time step, the iteration continues until the residuals were less than 10^{-6} for the mass and momentum equations, 10^{-8} for the k and ω equations, and 10^{-10} for energy equations. At the interfaces between the unsteady RANS model and the LES model, the vortex method was used to generate velocity fluctuation. A velocity inlet boundary condition was used with the velocity was estimated for $Re = 3000$, 4000 and, 5000 based on the throat hydraulic diameter. The inlet turbulence intensities were set 3%, 4%, and 5% for Re = 3000, 4000, and 5000, respectively. Though the heat transfer analysis of fluidic oscillators using air as the working fluid was seen in much open literature, the experimental results using water were absent. To validate the results of the simulations, the grid independence was checked for all the three designs. For the angled design, three grid systems with 6.08, 8.80, and 10.85 million grids were built. When Re = 5000, the oscillation frequencies of the device were 164, 167, and 166, respectively. For the curved design, three grid systems with grid number 5.80, 8.18, and 10.34 million were built. When Re = 5000, the oscillation frequencies were 165, 162, and 162, respectively. The simulation results were thought to be grid independent as the derivations of the oscillation frequency were less than 2.0% for all the simulation cases. The grid system using for the direct jet was the same to the angled design but with the two feedback channels removed, thus the simulation results of the direct jet were assumed grid independent. The simulation was performed for 100 non-dimensional time units (D/U_0) for each case. And the heat transfer data from the last three oscillation cycles were averaged as the final results.

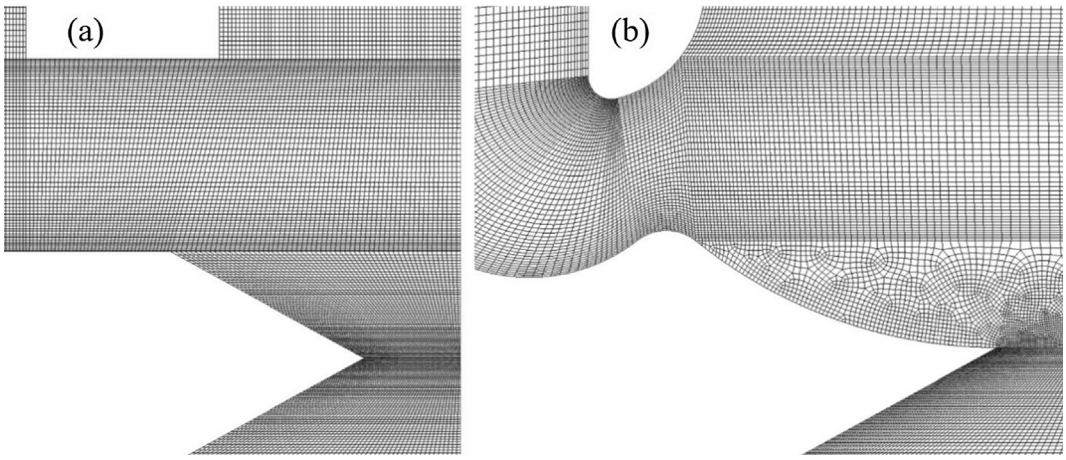

Fig. 3. The grid systems for (a) the angled design and (b) the curved design.

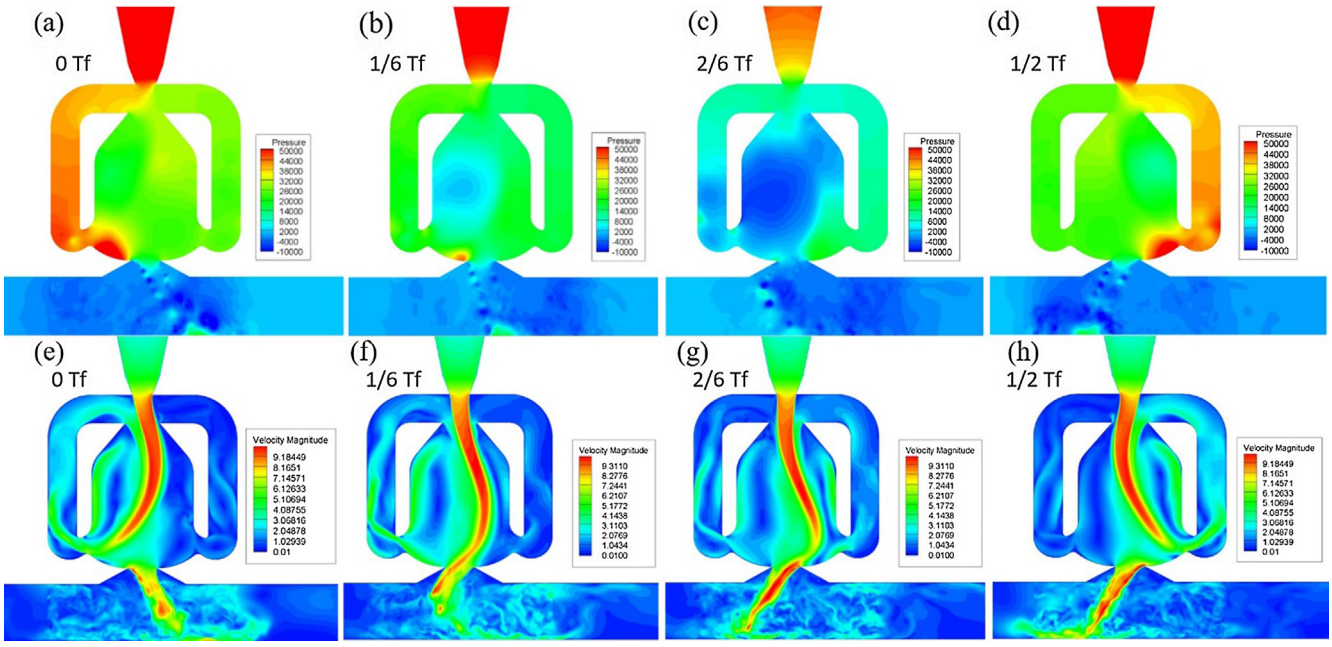

Fig. 4. (a)–(d) Instantaneous pressure contours and (e)–(h) flow patterns of the curved fluidic oscillator for one oscillation cycle when $Re = 5000$ (T_f is the period).

3. Results and discussion

3.1. The flow field and oscillation frequencies

As depicted in Figs. 4 and 5, a quasi-steady oscillatory flow pattern was observed for both two fluidic oscillator designs. The internal flow dynamics of the two fluidic oscillator designs has been intensively discussed in the previous experimental and numerical studies. The observed fluidic patterns in this study were nearly identical to those found in the open literature. Figs. 4 and 5 showed the instantaneous pressure and flow fields of the curved and the angled fluidic oscillators for half of the sweeping period with $Re = 5000$. The pressure and flow fields of the other half period were symmetric to this half period. Notably, Figs. 4 and 5 clearly showed that the interaction between the flows from the two feedback channels and the main jet in the inlet junction region initiated the switching of jet direction. At 0.0 T, the fluid jet was attached to the right side of the nozzle exit wall. This generated a pressure unbalance in the flow through the two feedback channels. As the flow in the right feedback channel was blocked, the pressure in the left feedback channel was much higher than that in the right channel. The relatively high pressure in the left feedback channel pushed the jet from the right side to the left side of the nozzle wall. However, because of the inertia, the jet in the mixing channel continued to sweep to the right side wall, as shown at 1/6 T_f. At 2/6 T_f, as the jet moved to the left side of the nozzle exit wall, the high-pressure region expanded into the right side of the mixing chamber and pushed the sweeping jet to the left side of the mixing chamber. At 1/2 T_f, the fluid jet was attached to the left side of the nozzle wall. As these processes repeated, the jet within the mixing chamber executed an oscillatory motion, thus generated a sweeping jet through the outlet throat. Careful observations on the pressure distributions of the two fluidic oscillators found that the curved design had more significant pressure fluctuation during an oscillation period. The more considerable pressure difference between the two feedback channels helped to enlarge the sweep-

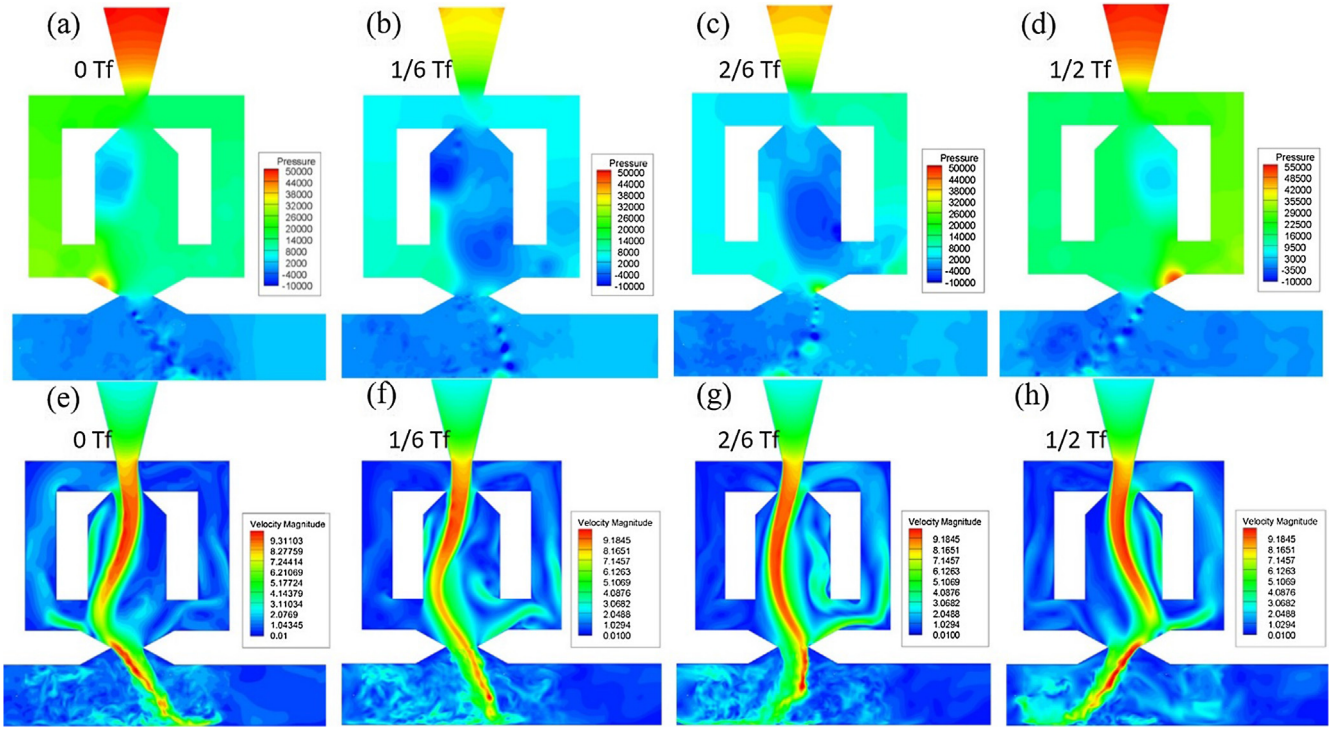

Fig. 5. (a)–(d) Instantaneous pressure contours and (e)–(h) flow patterns of the angled fluidic oscillator for one oscillation cycle when $Re = 5000$ (T_f is the period).

ing angle of the flow jet. As shown in Figs. 4(e)–(h) and 5(e)–(h), the curved design had a slightly larger sweeping angle than the angled design.

The oscillation frequency of the fluidic oscillator can be affected by many factors, such as the flow rate, feedback channel length, and working fluid. The oscillatory frequencies of the curved and the angled fluidic oscillators with $Re = 3000$, 4000, and 5000 were shown in Fig. 6. Though the difference in design, the oscillatory frequencies of the curved and angled designs were quite close to each other with the same *Re* number. The frequencies of the oscillatory jets almost linearly increased with the *Re* numbers for both designs. For the curved design, the oscillatory frequencies predicted by the ELES model and the $k-\omega$ SST model matched each other very well, with a difference of less than 4%. For the angled design, the ELES model predicted the oscillation frequencies slightly higher than the SST model for all the *Re* numbers. However, the difference became more significant for the cases with the higher *Re* numbers. In the main channel, the dynamic Smagorinsky model and *k-w* SST models were used to simulate the turbulence near and far away from the impinging zone, respectively. The LES model can provide more turbulence details. As observed in Figs. 4 and 5, the turbulence structures including the large scale and small scale eddies were clearly shown in the impinging zone. However, in the regions using the $k-\omega$ SST model, the small-scale eddies were filtered out. The turbulence eddies can play an essential role in the mass and energy transport due to the additional inertia stress and thermal fluxes. Oscillation of the jet flow created strong turbulence fluctuations and vortexes in the impinging zone. It was highly expected that the strong flow convection due to the turbulence fluctuations was able to enhance the convective heat transfer.

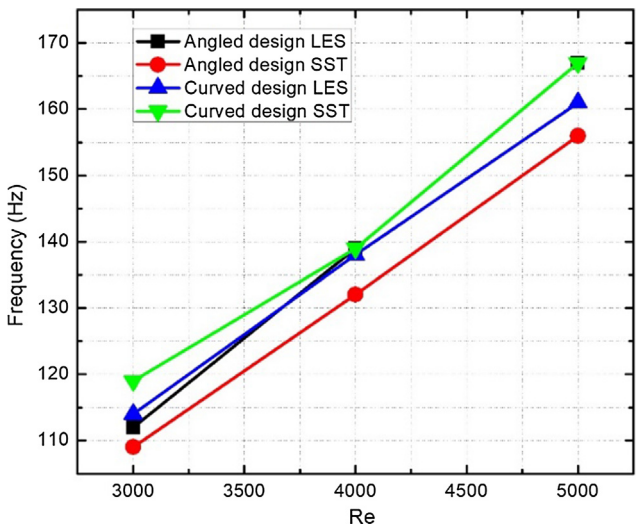

Fig. 6. The oscillatory frequency of the curved and angled designs at $Re = 3000$, 4000, and 5000.

3.2. Heat transfer results

It was well known that the turbulence introduced strong flow fluctuations and helped to destroy the boundary layers. It was reported in Refs. [8,27] that the intrinsic oscillation of the fluidic oscillator helped to enhance the overall convective heat transfer performance at the impinging zone. However, in some other literature [9], the sweeping jet did not show much advantage over the steady jet impingement in convective heat transfer, particularly near the impinging zone. The conclusions in the literature diverged. In this section, the problem was revisited and further clarified.

In this paper, a constant heat flux boundary condition, $q' = 1,000,000\ \mathrm{W/(m^2 \cdot K)}$, was set on the impinging wall. The time-averaged *Nu* number was compared for the three designs to see if oscillation of the jet can enhance the heat transfer performance. The *Nu* number was defined as

$$Nu = \frac{q' D_f}{\lambda (T - T_f)} \tag{11}$$

where the reference temperature was set to be 300 K and the hydraulic reference diameter was set to be 1.5 mm. The convective heat transfer coefficient related to *Nu* number via $h = \frac{Nu \cdot \lambda}{D_f}$.

Fig. 7(a)–(d) and (e)–(h) compared the instantaneous temperature contours of curved design using two different turbulence models. Strong turbulence fluctuations were observed in the impinging zones, particular for the LES model. As the turbulence indicated the contributions of additional fluid stresses and energy transfer due to oscillatory motion, the accuracy of the heat transfer simulation of the fluidic oscillators has heavily relied on the accuracy of the turbulence modeling. Turbulent flows were characterized by eddies with a wide range of length and time scales. The LES model was believed to be able to capture the details of the eddies within a wider length and time scales. As shown in Fig. 7, the temperature fluctuation was more clearly observed in simulation results using the ELES models. The strong turbulence fluctuation would increase convection and diffusion significantly, thus enhance the heat transfer process in the impinging zone. Fig. 7 (i)–(l) showed the instantaneous temperature contours of curved design simulated using the ELES model. The flow patterns of the curved design were quite similar to the angled design, but with smaller sweeping angles.

Fig. 8 showed the time-averaged surface *Nu* number contours on the jet impinging wall ($6.5 \times 1.5\ mm^2$) for the two sweeping and one direct jets at *Re* = 3000 and 5000. Data was averaged over three full-time periods for each case. Some distinct features were observed for the different fluidic designs. Different from the direct jet, two distinct peaks were observed for the sweeping jets due to the bi-stable nature of the fluidic oscillators. The region of the high *Nu* numbers shifted from the center of the impinging zone as the sweeping jet spends most of the time attached to one of the mixing

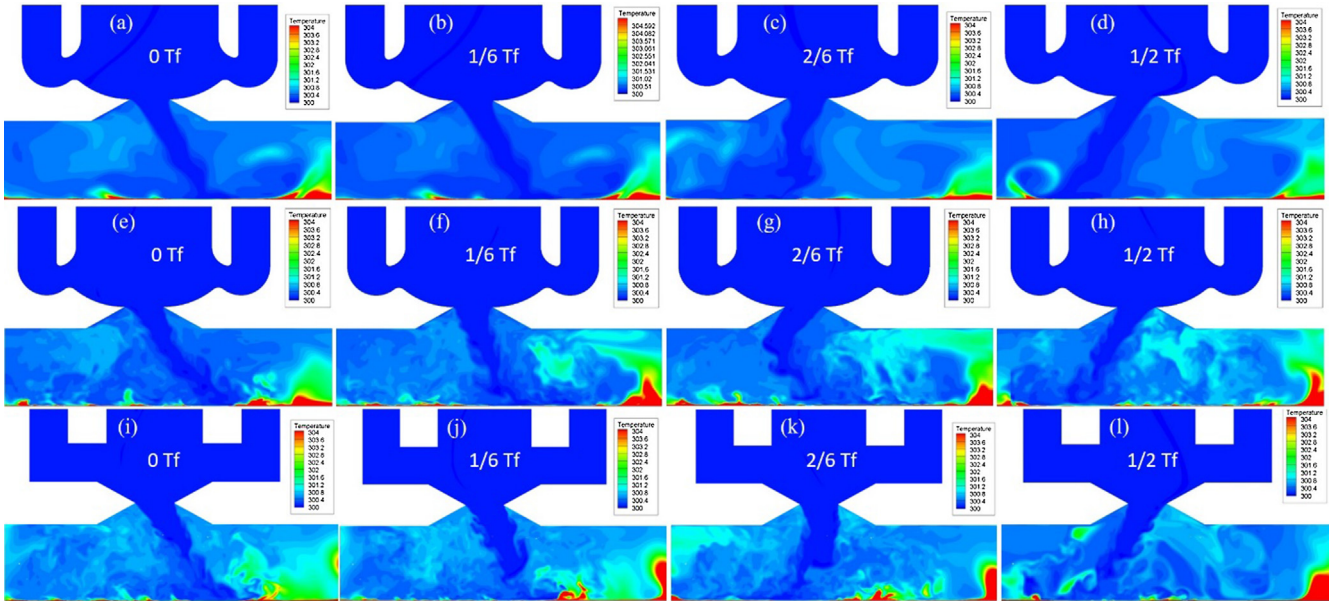

Fig. 7. (a)–(d) Instantaneous temperature contours of curved design using $k - \omega$ SST model. (e)–(h) Instantaneous temperature contours of curved design using ELES model. (i)–(l) Instantaneous temperature contours of angled design using ELES model. (T_f is the period).

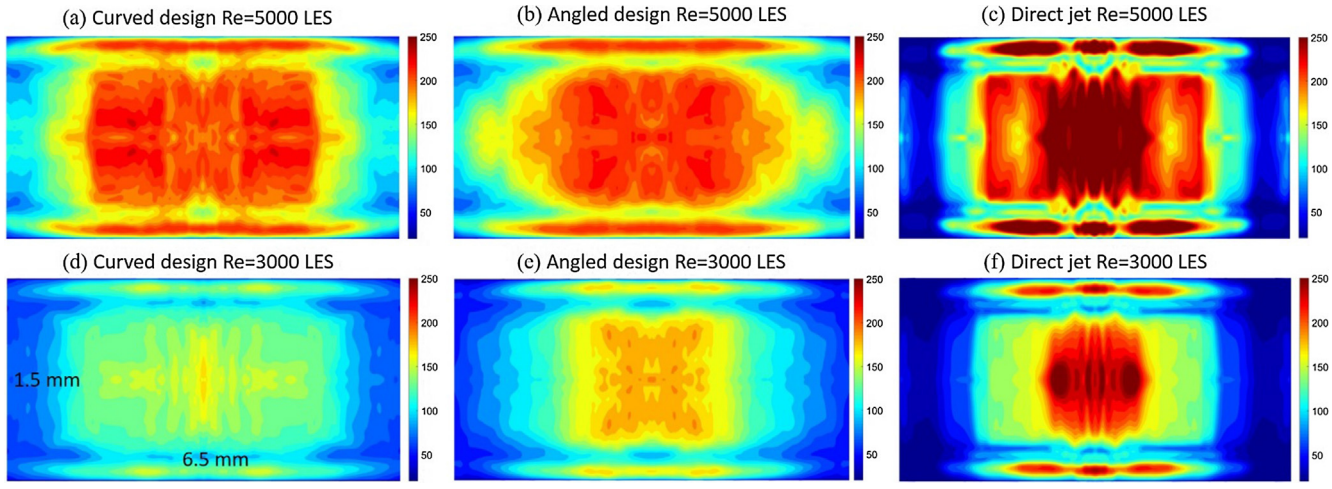

Fig. 8. (a)–(c) Time averaged *Nu* number contours on the impinging surface for the three designs at *Re* = 5000 using ELES model, (d)–(f) Time averaged *Nu* number contours on the impinging surface for the three designs at *Re* = 3000 using ELES model.

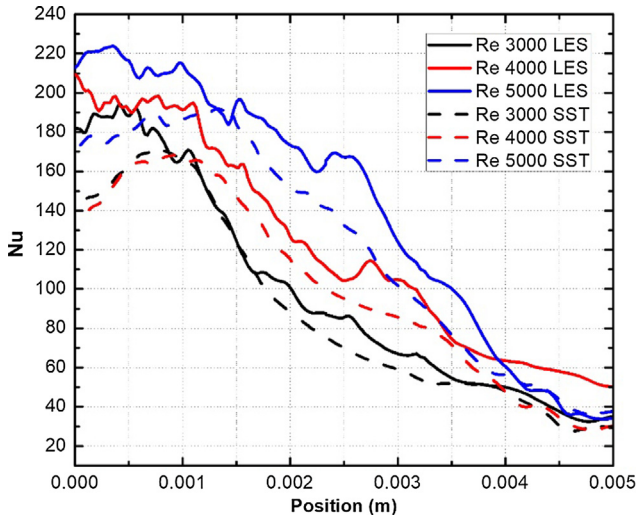

Fig. 9. Time averaged surface *Nu* distribution for sweeping jet on the channel centerline at *Re* = 3000, 4000, and 5000 for the curved design.

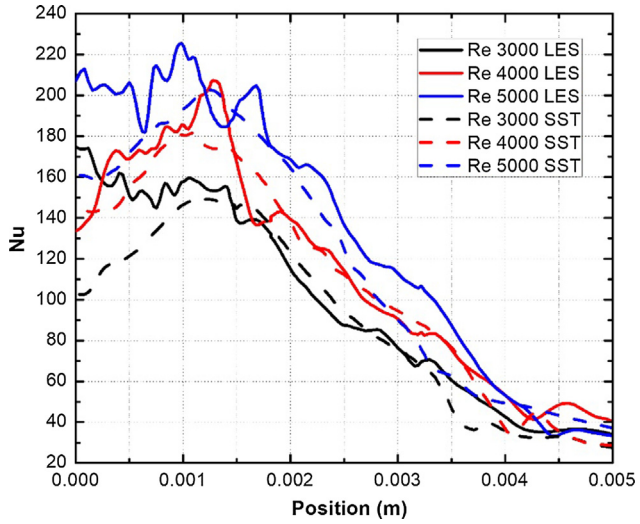

Fig. 10. Time averaged surface *Nu* distribution for sweeping jet on the channel centerline at *Re* = 3000, 4000, and 5000 for the angled design.

Table 1
The average *Nu* numbers over the impinging surface (6.5×1.5 mm^2).

Re	Curved design	Angled design	Direct jet
3000	112.60	118.74	109.34
4000	143.23	141.65	131.52
5000	167.40	165.96	154.53

chamber walls. As shown in Fig. 8, the distance between the high-*Nu*-number spots became further to each other with the higher *Re* number. Meanwhile, the coverage area of the impinging jet increased with *Re* number, as a larger high-*Nu*-number zone illustrated in Fig. 8 for *Re* = 5000. For *Re* = 3000 or 5000, the curved design, the angled design, and the direct design owned a relatively wide, medium, and narrow high-*Nu*-number zone on the impinging wall. Near the vertical wall of the channel, two long and narrow high *Nu* zones were observed because of the interaction between the turbulence flow and the walls. Though the direct jet owned a relatively narrow high-*Nu*-number zone, the maximum *Nu* number of the direct jet was larger than the sweeping jets. Overall, the heat

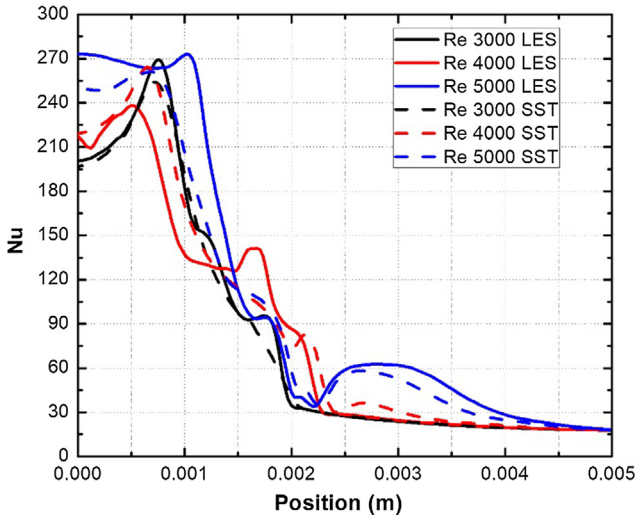

Fig. 11. Time averaged surface *Nu* distribution for sweeping jet on the channel centerline at *Re* = 3000, 4000, and 5000 for the direct jet design.

transfer performance of the fluidic oscillators increased with the *Re* number. This was reflected in both the more uniform *Nu* contours and higher average *Nu* numbers, as shown in Table 1. When compared with the direct jet, the curved design demonstrated a 3.0–8.3% increase in the heat removal performance, while the angled design represented a 7.4–8.6% increase. Implementing self-oscillating fluidic oscillators showed promising heat transfer enhancement for different *Re* numbers.

As shown in Figs. 9–11, overall, the *Nu* number distribution on the centerline of the channel predicted by the ELES model and the SST model matched each other very well for different *Re* numbers. Both turbulence models predicted higher *Nu* numbers with larger *Re* numbers. The $k-\omega$ SST model predicted two distinct *Nu* number peaks for the sweeping jets, while the peaks were not clear for the cases simulated using the LES model. The *Nu* number distributions simulated using $k-\omega$ SST model were smoother than LES model, as the turbulence fluctuations introduced extra energy fluxes thus affected the heat transfer process. As observed in Figs. 9–11, the *Nu* number distributions on the centerline of the channel decreased from the center to the side. For the direct jet, the *Nu* number decreased shapely along the centerline, while the decreasing tend was smoothly for the sweeping jets. It should be noted that the simulation result for the direct jet was different from that reported in the open literature where the maximum heat transfer coefficient happened at the center of the impinging zone. As shown in Fig. 11, the maximum heat transfer point slightly offset the center of the impinging zone. This can be reasoned by the unique divergent shape of the outlet throat.

4. Conclusion

Unsteady RANS and ELES simulations were performed to evaluate the impinging heat transfer performance of two self-oscillating fluidic oscillators and one direct jet. The results with different *Re* numbers were compared. The time-resolved pressure and flow fields were examined to understand the unsteady flow structure. To evaluate the heat transfer performance, the time-resolved temperature fields obtained by different turbulence models were compared. The time-averaged *Nu* numbers on the impinging surface were studied. Some key findings were summarized in the following:

(1) The numerical analysis of the fluid dynamics in the fluidic oscillators suggested that the jet deflection was initiated by the pressure difference within the two feedback channels. Then the jet deflection propagated downstream and formed the sweeping behavior in the mixing chamber and the outlet throat. The curved fluidic oscillator owned a larger pressure fluctuation than the angled design. Thus sweeping jet in the curved fluidic oscillator covered a larger impinging zone.

(2) Both the $k-\omega$ SST model and the ELES model were used to conduct the turbulence simulations. Overall, the fluid dynamics and frequencies predicted by the two models matched each other reasonably well for different *Re* numbers.

(3) The averaged heat transfer performance of the jets for all these three designs increased with *Re* numbers. The direct impinging jet had better heat transfer performance at the center of the impinging zone. However, its performance deteriorated sharply offset the center. The sweeping jets aroused by the fluidic oscillators had a better average and more uniform heat removal performance. The curved design demonstrated a 3.0–8.3% increase in the heat removal performance, while the angled design represented a 7.4–8.6% increase with Re number ranging from 3000–5000.

(4) The heat removal performance predicted by the $k-\omega$ SST model and the ELES model matched very well for all the cases. Two *Nu* number peaks were observed in the results obtained using the $k-\omega$ SST turbulence model. The *Nu* numbers calculated by the ELES model fluctuated more significantly near the impinging zone due to the extra energy flux transport by the small eddies. Because of the strong turbulence, the two *Nu*-numbers peaks tended to emerge with each other and formed a sizable high-*Nu*-number zone on the impinging surface.

The unsteady characteristics of fluidic oscillators are desirable for the development of the next-generation heat exchangers with extremely high heat flux removal capacity. For example, as reported in Refs. [34,35], multi-phase heat exchangers made by synthetic diamond integrated with a phase separation concept was used to design high-performance heat sinks with thermal conductivity exceeding 1000 $W/(m \cdot K)$. It was observed that the venting rate was critical for the phase separation thus affected the heat transfer performance. Also, the dry-out phenomenon was reported as a main obstacle for further heat transfer improvement. It is highly expected that the fluidic oscillators can help to improve the gas venting and alleviating the dry-out phenomenon by separating the bubbles attached to the heating surface. It is also promising to significantly enhance the heat removal capacity of the heat exchangers by adjusting the inlet configurations of the heat exchangers using the fluidic oscillator arrays.

Conflict of interest

The authors declare that there is no conflict of interest.

Acknowledgement

The authors acknowledged the support of US National Science Foundation via Grant #1508862.

References

[1] R. Woszidlo, I. Wygnanski, Parameters governing separation control with sweeping jet actuators, in: 29th AIAA Applied Aerodynamics Conference, 2011, p. 3172.
[2] R. Woszidlo, H. Nawroth, S. Raghu, I. Wygnanski, Parametric study of sweeping jet actuators for separation control, in: 5th Flow Control Conference, 2010, p. 4247.
[3] G. Raman, S. Packiarajan, G. Papadopoulos, C. Weissman, S. Raghu, Jet thrust vectoring using a miniature fluidic oscillator, Aeronaut. J. 109 (1093) (2005) 129–138.
[4] G. Raman, S. Raghu, Cavity resonance suppression using miniature fluidic oscillators, Aiaa J. 42 (12) (2004) 2608–2612.
[5] M. Metka, J.W. Gregory, Drag reduction on the 25-deg Ahmed model using fluidic oscillators, J. Fluid Eng.-Trans. Asme 137 (5) (2015).
[6] D. Guyot, B. Bobusch, C.O. Paschereit, S. Raghu, Active combustion control using a fluidic oscillator for asymmetric fuel flow modulation, in: 44th AIAA/ASME/SAE/ASEE Joint Propulsion Conference & Exhibit, 2008, p. 4956.
[7] L. Agricola, R. Prenter, R. Lundgreen, M. Hossain, A. Ameri, J. Gregory, J. Bons, Impinging sweeping jet heat transfer, in: 53rd AIAA/SAE/ASEE Joint Propulsion Conference, 2017, p. 4974.
[8] C. Camci, F. Herr, Forced convection heat transfer enhancement using a self-oscillating impinging planar jet, J. Heat Transfer-Trans. Asme 124 (4) (2002) 770–782.
[9] M.A. Hossain, L. Agricola, A. Ameri, J.W. Gregory, J.P. Bons, Effects of curvature on the performance of sweeping jet impingement heat transfer, in: 2018 AIAA Aerospace Sciences Meeting, 2018, p. 0243.
[10] M.A. Hossain, R. Prenter, R.K. Lundgreen, A. Ameri, J.W. Gregory, J.P. Bons, Experimental and numerical investigation of sweeping jet film cooling, J. Turbomach. 140 (3) (2018) 031009.
[11] R.W. Warren, Fluid oscillator, in, Google Patents, 1962.
[12] J. Gregory, M.N. Tomac, A review of fluidic oscillator development, in: 43rd AIAA Fluid Dynamics Conference, 2013, p. 2474.
[13] S. Raghu, Feedback-free fluidic oscillator and method, in, Google Patents, 2001.
[14] R.J. Englar, Overview of circulation control pneumatic aerodynamics: blown force and moment augmentation and modification as applied primarily to fixed wing aircraft, in: Proceedings of the 2004 NASA/ONR Circulation Control Workshop, NASA CP-2005-213509, 2005, pp. 23–66.
[15] L.N. Cattafesta III, M. Sheplak, Actuators for active flow control, Annu. Rev. Fluid Mech. 43 (2011) 247–272.
[16] J.H. Seo, R. Mittal, Computational modeling and analysis of sweeping jet fluidic oscillators, in: 47th AIAA Fluid Dynamics Conference, 2017, p. 3312.
[17] J. Seo, C. Zhu, R. Mittal, Flow physics and frequency scaling of sweeping jet fluidic oscillators, AIAA J. (2018) 1–12.
[18] M.A. Hossain, R. Prenter, L. Agricola, R.K. Lundgreen, A. Ameri, J.W. Gregory, J.P. Bons, Effects of roughness on the performance of fluidic oscillators, in: 55th AIAA Aerospace Sciences Meeting, 2017, p. 0770.
[19] B.C. Bobusch, R. Woszidlo, J.M. Bergada, C.N. Nayeri, C.O. Paschereit, Experimental study of the internal flow structures inside a fluidic oscillator, Exp. Fluids 54 (6) (2013).
[20] J.W. Gregory, E.P. Gnanamanickam, J.P. Sullivan, S. Raghu, Variable-frequency fluidic oscillator driven by a piezoelectric bender, AIAA J. 47 (11) (2009) 2717–2725.
[21] R. Woszidlo, T. Stumper, C. Nayeri, C.O. Paschereit, Experimental study on bluff body drag reduction with fluidic oscillators, in: 52nd Aerospace Sciences Meeting, 2014, p. 0403.
[22] M.N. Tomac, J.W. Gregory, Internal jet interactions in a fluidic oscillator at low flow rate, Exp. Fluids 55 (5) (2014).
[23] F. Ostermann, R. Woszidlo, C. Nayeri, C.O. Paschereit, Experimental comparison between the flow field of two common fluidic oscillator designs, in: 53rd AIAA Aerospace Sciences Meeting, 2015, p. 0781.
[24] H.S. Jeong, K.Y. Kim, Shape optimization of a feedback-channel fluidic oscillator, Eng. Appl. Comp. Fluid 12 (1) (2017) 169–181.
[25] T. Choephel, J. Coder, M. Maughmer, Airfoil boundary-layer flow control using fluidic oscillators, in: 30th AIAA Applied Aerodynamics Conference, 2012, p. 2655.
[26] M. DeSalvo, E. Whalen, A. Glezer, High-lift enhancement using fluidic actuation, in: 48th AIAA Aerospace Sciences Meeting Including the New Horizons Forum and Aerospace Exposition, 2010, p. 863.
[27] T. Park, K. Kara, D. Kim, Flow structure and heat transfer of a sweeping jet impinging on a flat wall, Int. J. Heat Mass Transf. 124 (2018) 920–928.
[28] M. Germano, U. Piomelli, P. Moin, W.H. Cabot, A dynamic subgrid-scale eddy viscosity model, Phys. Fluids A 3 (7) (1991) 1760–1765.
[29] A. Fluent, Theory Guide and User's Guide, Ansys Inc, USA, 2015.
[30] R. Seele, E. Graff, J. Lin, I. Wygnanski, Performance enhancement of a vertical tail model with sweeping jet actuators, in: 51st AIAA Aerospace Sciences Meeting including the New Horizons Forum and Aerospace Exposition, 2013, p. 411.
[31] F.R. Menter, M. Kuntz, R. Langtry, Ten years of industrial experience with the SST turbulence model, Turbul. Heat Mass Transfer 4 (1) (2003) 625–632.
[32] F.R. Menter, Performance of popular turbulence model for attached and separated adverse pressure gradient flows, AIAA J. 30 (8) (1992) 2066–2072.
[33] D.K. Lilly, A proposed modification of the Germano subgrid-scale closure method, Phys. Fluids A 4 (3) (1992) 633–635.
[34] M.P. David, J. Miler, J.E. Steinbrenner, Y.Z. Yang, M. Touzelbaev, K.E. Goodson, Hydraulic and thermal characteristics of a vapor venting two-phase microchannel heat exchanger, Int. J. Heat Mass Transf. 54 (25–26) (2011) 5504–5516.
[35] M.P. David, J.E. Steinbrenner, J. Miler, K.E. Goodson, Adiabatic and diabatic two-phase venting flow in a microchannel, Int. J. Multiph. Flow 37 (9) (2011) 1135–1146.